nature materials

INSIGHT | REVIEW ARTICLES

PUBLISHED ONLINE: 24 MARCH 2009 | DOI: 10.1038/NMAT2400

# Coherent X-ray diffraction imaging of strain at the nanoscale

Ian Robinson[1]* and Ross Harder[2]

**The understanding and management of strain is of fundamental importance in the design and implementation of materials. The strain properties of nanocrystalline materials are different from those of the bulk because of the strong influence of their surfaces and interfaces, which can be used to augment their function and introduce desirable characteristics. Here we explain how new X-ray diffraction techniques, which take advantage of the latest synchrotron radiation sources, can be used to obtain quantitative three-dimensional images of strain. These methods will lead, in the near future, to new knowledge of how nanomaterials behave within active devices and on unprecedented timescales.**

X-ray diffraction methods lie at the foundation of materials science. Determination of the crystal structures of natural minerals and, later, of crystals grown in the laboratory led to our considerable understanding of chemical bonding and cohesion that is the basis of the solid-state sciences[1]. Nanoscale materials are emerging that have promising new properties, many of which are associated with previously unknown structures, quantifiable as strains that can be detected by X-ray methods. Here we review some of the advances in X-ray diffraction methods and their augmentation with the use of the laser-like beams available at the latest sources of synchrotron radiation, which are now providing spatially resolved structures of nanoscale objects. We will specifically explain the isostrain method, high-resolution methods and coherent X-ray diffraction methods.

Nanomaterials are defined as those with crystal grain sizes in the range of 100 nm or less. Such materials can possess properties remarkably different from their bulk counterparts, most obviously detected as reduced melting points[2], enhanced reactivities[3] or significantly modified electronic band structures[4]. Numerous applications of these new properties are being developed in the new field of nanotechnology. The simplest explanation of why the properties of nanocrystals differ from the bulk is that a considerable fraction of the volume of nanocrystals lies close to external surfaces and interfaces. The different chemical and physical properties of those surfaces therefore dominate the bulk behaviour.

Strain is the physical concept used to describe the structural deviation of the crystal from the ideal bulk state. It is defined as the spatial derivative of the displacement of the material from an ideal lattice, and hence has a tensorial nature. It is connected through elasticity theory with stress, which is generally thought to be the origin of strain and can arise from chemical, electrical, magnetic, mechanical and other forces associated with the local environment of the crystal. Because of the enhanced role of their surfaces, strain in nanomaterials is expected to be significantly enhanced relative to bulk materials, thus opening significant opportunities for nanotechnology. In this review, we illustrate how strain in nanomaterials can be measured using X-ray diffraction.

A strong reason for developing the capability to image strain in nanocrystals in the context of materials science is that the strain can be altered substantially by processing of the material, either as part of its designed function or to test fundamental materials science principles. Shock waves, ion irradiation tracks, chemical modification or external fields applied to a crystalline grain are all expected to cause characteristic patterns of strain, often with associated domain formation on the nanoscale. Classical defect structures, such as free dislocations, dislocation loops and stacking-fault tetrahedra all have characteristic strain fields that can be used to identify the defect modes present, given sufficient resolution. Whereas pure elasticity effects are expected to behave according to classical theory down to a very small size scale, this is not the case for plasticity. Yield stresses are found to increase substantially in crystal grains smaller than a micrometre and continue to deviate on the nanoscale, following a 'smaller is stronger' trend[5]. The complete understanding of such trends demands suitable methods of strain imaging on the nanoscale.

Looking to the future, imaging of strain dynamics[6] associated with transients on the femtosecond timescale will become possible once the planned hard-X-ray free-electron lasers start operating. The experimental methods under development today, as described in this article, will become the methods of choice for producing single snapshots of excited matter at the future facilities[7]. A shock wave would completely traverse a 100-nm crystal in 100 ps, allowing plenty of opportunity to reveal its evolution at the expected time resolution of 100 fs. Crystallographic 'difference map' methods applied to fully phased starting structures will be very effective for examining localized changes in single-shot applications that can destroy the sample.

X-ray diffraction methods are by no means the only method of measuring strain distributions on the nanoscale. Transmission electron microscopy (TEM) and related off-axis electron holography methods[8] can achieve higher resolution than current X-ray methods and may also be quantitative. Transmission electron microscopy methods are reviewed in a companion article[9]. Both methods measure strain as a phase, but one slight distinction is that X-ray diffraction measures the three-dimensional (3D) distribution of a particular component of the strain field whereas electron holography measures the vector strain field in a particular projection. Conventional[10] and aberration-corrected[11,12] TEM can also map strain at high resolution by direct imaging. Furthermore, TEM can be used to map both the strain and its relationship to the surrounding device structure that contains it[13].

Scanning probe X-ray methods are also not reviewed here. Spectroscopic methods, reviewed in a related article in this Insight[14], are not directly sensitive to strain. Newly implemented ptychographic methods[15,16] could be made sensitive to strain, which would appear as a complex density (see below), by introducing Bragg

[1]London Centre for Nanotechnology, University College, 17–19 Gordon Street, London WC1H 0AH, UK and Diamond Light Source, Harwell Campus, Didcot, Oxfordshire OX11 0DE, UK. [2]Advanced Photon Source, Argonne, Illinois 60439, USA.*e-mail: i.robinson@ucl.ac.uk

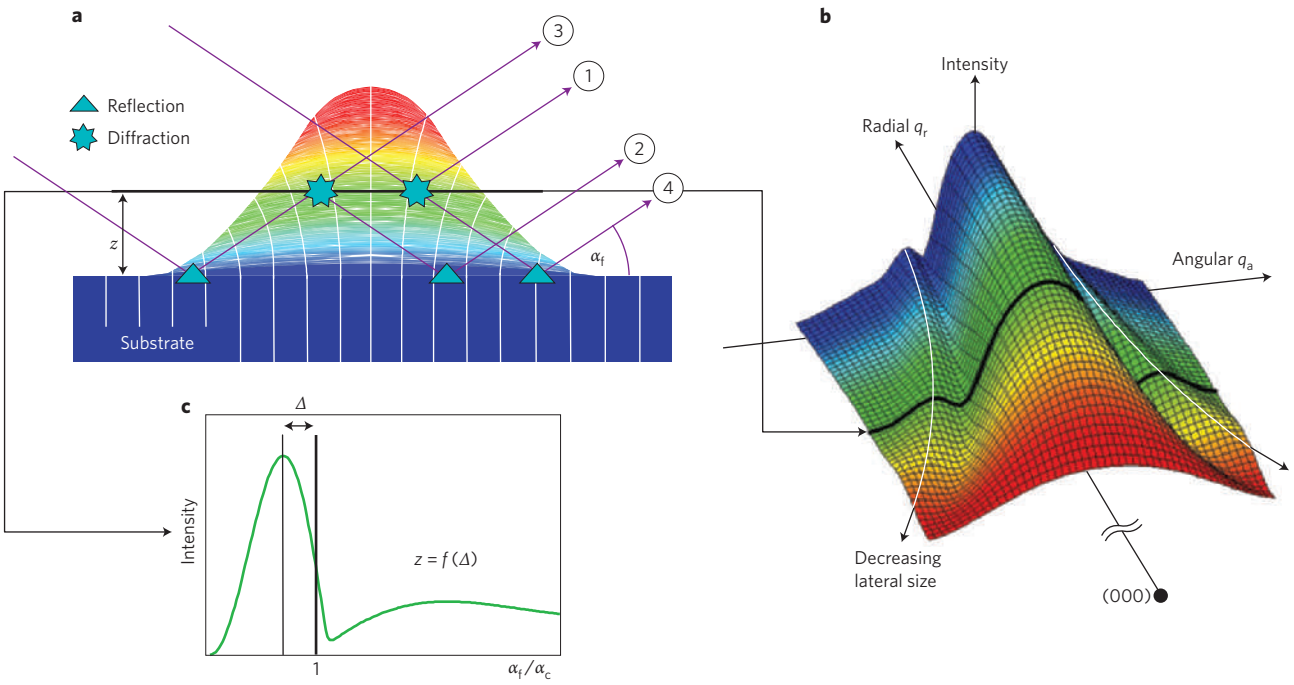


**Figure 1 | Schematic of the isostrain method used to measure the strain inside quantum dot structures[30].** The illustration shows how a slice at a given height in the quantum dot is cut out by measuring the transverse diffraction profile at a radial momentum transfer ($q_r$) corresponding to the dot's lattice parameter there. **a**, Cross-section of a quantum dot in which the lattice parameter increases from the bottom to the top. **b**, Diffraction pattern of the quantum dot, close to one of the substrate reflections. The deviation along the radial $q_r$ direction (black slice along the $q_a$ direction and colour coding) identifies the contribution from a particular height $z$, in the structure. **c**, Intensity as a function of the exit angle $\alpha_f$ in units of the critical angle $\alpha_c$. The shift of the maximum $\Delta$,is characteristic of the height $z$, assuming contributions from all paths 1 to 4. Figure reprinted with permission from ref. 21. © 2005 Elsevier.

diffraction, but this has not been reported yet. The most important strain-sensitive scanning instruments are the white-beam Laue scanning microprobe[17], beamline 34-ID-E at the Advanced Photon Source (APS), Argonne National Laboratory, Illinois, which can measure the full strain tensor at every measurement point, and the Risø X-ray microscope[18], beamline ID11 at the European Synchrotron Radiation Facility (ESRF), Grenoble. These have been reviewed previously[19]. We also do not discuss any of the forward-scattering lensless-imaging X-ray work, stemming from the experiment of ref. 20, which uses the same phasing principles, because these techniques are also insensitive to strain.

A current challenge to the field is the synthesis of well-isolated structures with some indexing system that would allow the same crystal to be probed by a number of methods. Most importantly, this would allow the same crystal to be compared before and after some treatment is applied. It is to be expected that far more information (about shape and strain) would be obtained for a single particle than for an average over a distribution of slightly different ones, even if they could all be made to have the same crystallographic orientation. This follows the current trend away from interest in thermodynamic average properties towards studying transient and extremely excited systems far from equilibrium. An important practical consideration is that single-particle methods avoid all the limitations of preparing artificially monodispersed samples.

## Strain in quantum dots

Pattern formation in epitaxial systems of semiconductors has been studied using X-ray diffraction, mostly without using the coherence properties directly. Extensive work spanning many years has been published by the groups of Bauer, Stangl and Holy, mostly using beamline ID01 of the ESRF, run by the group of Metzger[21-27]. Whenever there is lattice mismatch between a thin film of one semiconductor and its substrate, there is a maximum (critical) thickness of strained material that can form[28]. The classical example is Ge on Si with a 4% lattice mismatch and a critical thickness around 1 nm, rising to 100 nm for $Ge_{0.2}Si_{0.8}$ alloy[29]. Critical-thickness effects are now a mainstream concept in materials science[28]. Films greater in thickness than the critical value enter a Stranski–Krastanov growth mode that eventually leads to isolated islands of relaxed material, familiarly known as quantum dots because their size (20–100 nm) is correct for the quantum confinement of electrons.

We highlight the isostrain method[30], which has shown that such free-standing islands are highly strained with respect to the substrate. This method, illustrated in Fig. 1, is based on grazing-incidence diffraction from a large population of free-standing (not buried) quantum dots, epitaxially grown on a substrate with a narrow (<10%) size distribution. As illustrated, it assumes a monotonic variation of lattice parameter with height inside the quantum dot, as expected from its varying composition and strain relaxation. The transverse diffraction profile (Fig. 1b) at each radial position, denoted $q_r$, in the vicinity of an in-plane Bragg peak is the Fourier transform of the shape of the crystal with that particular lattice constant; the exit-angle ($\alpha_f$) profile perpendicular to the surface (Fig. 1c) is explained by taking into account the four diffraction paths shown in Fig. 1a (ref. 30). The isostrain method has been extended by combining it with resonant scattering and analysing the intensity profile along the transverse direction to reveal the 3D composition and strain profile in SiGe quantum dots on Si (ref. 31).

Recent work has applied the isostrain method to island 'molecules' of InAs quantum dots that form binary pairs aligned with the substrate directions[22], pattern formation on GaSb(001) by ion-beam sputtering[23] and strong chemical ordering effects in GeSi alloys on Si that couple to the strain fields[24-27]. The unique characteristic of the last work is that the induced chemical ordering is

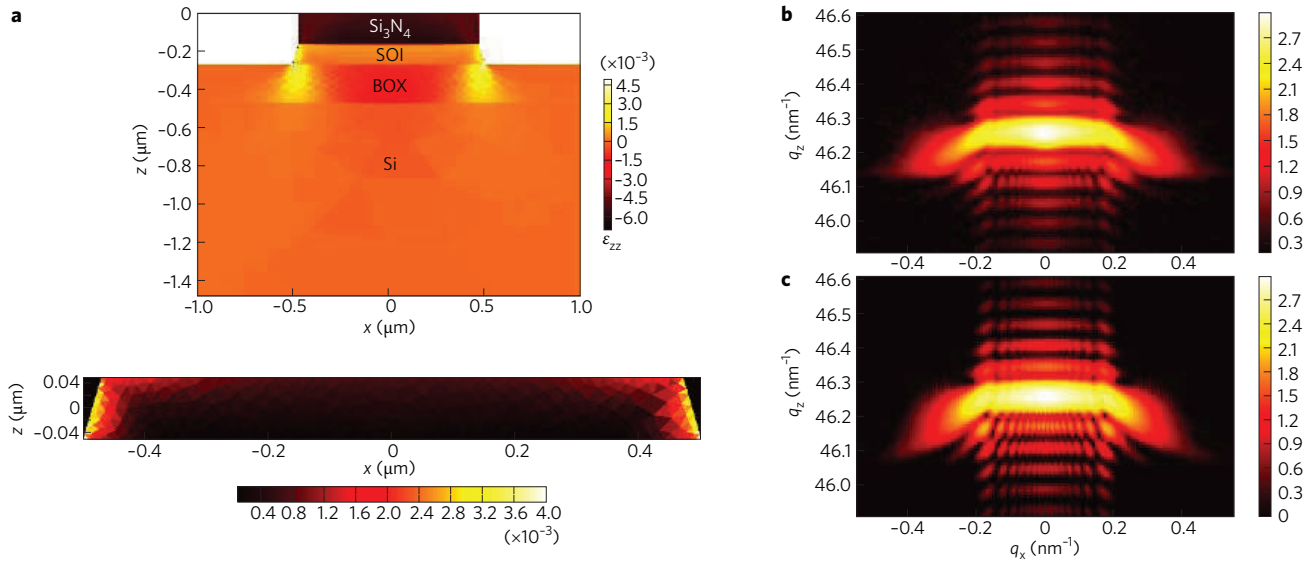


**Figure 2 | Strain due to patterning of silicon. a**, *xz* cross-section of the measured structure showing the FEA calculation of the $\varepsilon_{zz}$ strain component shown on the indicated colour scale. A magnified view of the silicon on insulator (SOI) portion is shown below on a finer colour scale. The supporting oxide layer is denoted BOX. **b**, Measured diffraction pattern surrounding the 004 reflection of the SOI structure as a function of its $q_x$ and $q_z$ components. **c**, Corresponding diffraction pattern calculated for the structure shown in **a**. Figure reprinted with permission from ref. 33. © 2007 AIP.

visible at the otherwise forbidden (200) reflection[25]. An important limitation of this X-ray work so far is the need to average the data over a large number of quantum dots, which have to be made with the same shape and similar size, with identical orientations on the substrate. The situation is helped by the tendency of the islands to self-assemble at a particular size determined by the strain of the misfit with the substrate. In the most recent work, a microfocused beam was used to isolate the contributions of individual quantum dots[27]. The size distribution can also be controlled by suitable patterning of the starting substrate, which leads to various applications in nanotechnology[32].

## Strain due to lithographic patterning

Another perspective of strain measurement using X-rays comes from the group of Thomas at the Centre National de la Recherche Scientifique IM2NP laboratory in Marseille[33,36,37]. They have used high-resolution X-ray diffraction to examine the strain distributions in lithographically prepared micrometre-size structures composed as arrays to enhance the signal[33]. Finite element analysis (FEA) methods were used to model the strain, followed by a kinematical diffraction calculation. Like the quantum dot work mentioned above, the structures correspond to an array and are averaged over its periodicity. No attempt was made to model the properties of this artificial lattice, but only the shape and strain of the Si bars within it, which results in the intensity distribution of the diffraction. It was argued[33] that very small deviations from ideal periodicity cause the smearing out of any ultrafine fringes that would arise from the entire array.

The example shown in Fig. 2 is from a patterned structure engraved in a silicon-on-insulator (SOI) layer lying on its buried oxide substrate and underlying bulk Si handle. An array of 1-μm-wide wires, spaced 2 μm apart, was cut in the SOI (100 nm of Si on 200 nm of $SiO_2$) using a silicon nitride lithography mask. After reactive ion etching, the wire structures are left standing on the bare oxide substrate as illustrated in Fig. 2. A residual stress of 1.5 GPa remains in the silicon nitride layer, causing significant distortions in the Si wire, calculated using FEA, as shown. The kinematical diffraction pattern of the strained wire, shown in Fig. 2c, is in good agreement with the experimental data in Fig. 2b.

Again, averaging is used to increase the signal in the experiment, which was carried out at BM32, a bending magnet beamline at ESRF. Slight disorder in the relative positions of the wires making up the array removes any effect of interference between them; the limited coherence of the BM32 beam, in the range of several micrometres, would not be enough to achieve this. However, as the wires are effectively floating on amorphous oxide, it is reasonable that any spatial correlations present in the parent SOI layer would be lost.

The silicon nitride stress of 1.5 GPa that was found to explain the observations is a relatively large value. Without stress, the SOI wires would give diffraction patterns extending less than one-twentieth of the width seen in Fig. 2. In effect, many 'phase wraps' are present in the structure (see below). The X-ray methods discussed here are sensitive to stresses orders of magnitude smaller than this, yet use of the fabrication method of ref. 33 is not uncommon in the construction of semiconductor devices and 'strain engineering' is a powerful method of producing high-performance semiconductor devices[34]. Today's semiconductor industry is producing devices with feature sizes ('design rules') of 45 nm; at this level the resulting strain associated with the chemically processed interfaces will be much greater than those identified by ref. 33. At some point, the FEA bulk modelling will start to break down as the specific structural details of the crystal interfaces become relevant[35], as may already be the case at 45 nm. Other work by the same group has applied the method to Si trench-array structures[36] and succeeded in using iterative direct-phasing methods (described below) to obtain spatial images of the strain[37].

In future, strain patterns could be created in model devices with sizes more relevant to current technology (45 nm) that only partly penetrate the thickness of the SOI layer, or else in GeSi, as is relevant. For example, strain on the scale addressable with X-rays are expected to result from local heating in the channels of active model transistors. The embedding environment of a real device will also create strain. As the IM2NP group has found, it is important to use SOI methods because the active layer of Si has a different orientation from the much thicker handle; the diffraction of interest would be in the shape of the 111 or 220 Bragg peak of the layer, which would be completely swamped by the bulk substrate diffraction if SOI technologies were not used[33].

NATURE MATERIALS DOI: 10.1038/NMAT2400

**Box 1 | Solving the phase problem by CXD.**

The phasing of the data is a critical step that uses a computer algorithm that is illustrated schematically. The algorithm takes advantage of internal redundancies in the diffraction data when the measurement points are spaced close enough together to meet the 'oversampling' requirement[39]. Fourier transforms ('F'; fast Fourier transforms in the computer implementation) connect real-space arrays of data (left panels) with reciprocal space arrays (right panels). Both sides are updated in every cycle of the algorithm. Inputs to the algorithm are the measured intensity data (array amplitudes overwritten in the bottom-right panel) and a postulated 3D 'support' volume (translucent box in the top-left panel) in which all the complex sample density is constrained to exist. The measurement of diffraction data is shown schematically on the right: a narrow, coherent X-ray beam illuminates one of the Pb nanocrystals grown (*in situ*) on a substrate (viewed subsequently by SEM) to produce a diffraction pattern on an area detector. The dimensions of the support can be estimated directly from the fringe spacings of the observed pattern or using autocorrelation methods. A technique known as 'shrink wrap' is sometimes used to allow the support to evolve on successive cycles as the algorithm progresses[55]. The oversampling condition is simply that the number of measurement points be at least twice the number of unknown density values within this support, as proposed in ref. 56 immediately after the publication of the Shannon theorem[57]. It was shown in ref. 58 that this is a sufficient condition for a unique set of phases to be determined, in two or more dimensions. The best known method for finding those phases and avoiding 'stagnation' problems is the hybrid input–output method[59], which starts with a random phase 'seed' and propagates a weighted combination of the current and previous cycles on the real-space side of the algorithm. This support-constrained phasing of the diffraction patterns of small objects is judged to be reliable because the same structure emerges from different random starting phase sets[60]. One measure of its reliability is that only 50 iterations of hybrid input–output are often enough to yield a consistent result with good data, whereas an earlier version of phasing algorithms required several thousand[61].

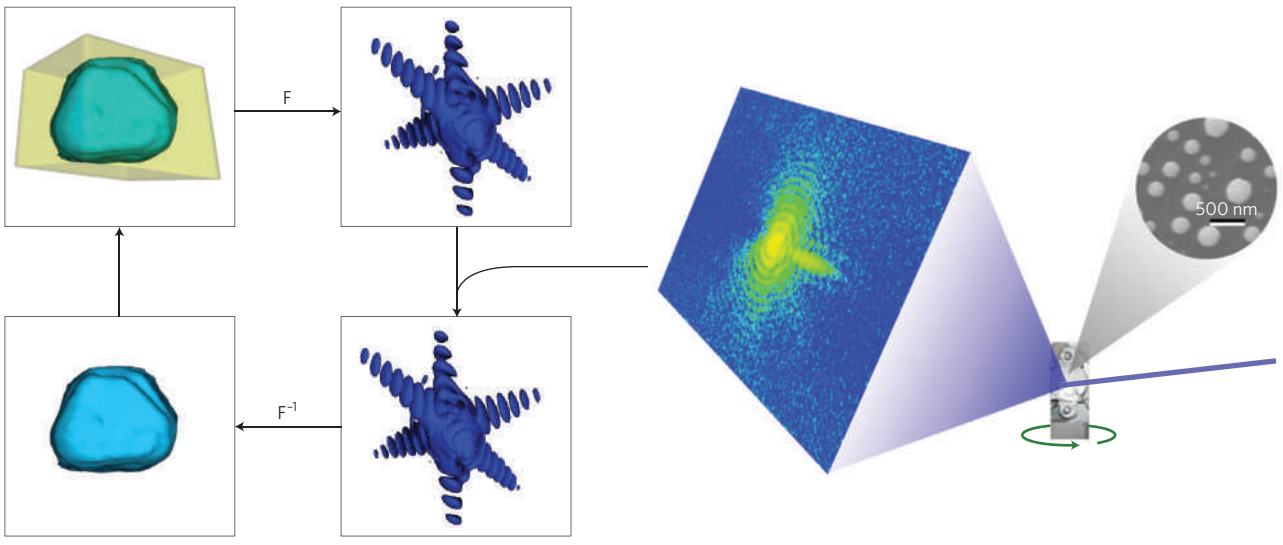


## Coherent X-ray diffraction

The sample-averaging limitations of the two methods described so far have been overcome by the development of coherent X-ray diffraction (CXD) as a 3D structural analysis method for individual small crystals. As explained in Box 1, the inversion of the diffraction pattern yields a 3D image of the density distribution of the sample and a projection of the strain within it, so it is a genuine form of phase-contrast X-ray microscopy. The basic principle of the CXD experiment is the illumination of the sample by a spatially coherent beam of X-rays, meaning that the transverse coherence length (of up to a few micrometres) should exceed the dimensions of the sample. Under these conditions, scattering from all parts of the sample can be expected to interfere in the far-field diffraction pattern.

The coherence effects we exploit were first documented for hard X-rays in 1991 (ref. 38). Coherent X-ray diffraction is usually measured in the same way as a normal diffraction experiment, but with a high-resolution charge-coupled device (CCD) or other X-ray detector positioned far enough away to resolve the finest fringes, called 'speckles' by analogy with scattering of laser light. As discussed further below, the requirement of at least two detector pixel spacings per fringe also ensures an 'oversampling' condition[39]. Obtaining enough coherent flux is only practicable with the brightness of undulator-based 'third-generation' synchrotron radiation sources, such as the ESRF and APS, used for the CXD results reported here.

The crystal lattice introduces a powerful new constraint on the selection of a grain for imaging. A polycrystalline sample will have closely packed grains with numerous different orientations. Its Bragg diffraction will resemble that of a powder but, with a small enough beam and a typical grain size of around a micrometre, the individual grains can still be separated. Even highly textured samples can have orientations distributed widely enough that the grains can be distinguished. Once a Bragg peak is isolated and aligned, its internal intensity distribution can be recorded by means of a CCD at the end of a long detector arm. A 'rocking' series of CCD images, in which the crystal's angle to the beam is varied by a fraction of a degree around its Bragg peak, yields a complete 3D data set.

The 3D data are then inverted to form quantitative real-space images using a computational method for solving the phase problem, described in Box 1. This computation effectively replaces the objective lens in a traditional microscope. A typical CXD pattern is

shown, consisting of characteristic rings resembling the Airy pattern of a compact, solid object and modulated streaks attributed to its prominent facets. The average intensity decays rapidly away from the centre of the Bragg peak, eventually reaching the background level of the detector. This radial cut-off determines the spatial resolution of the resulting real-space image. This is limited, in practice, by the counting statistics, but more by the stability of the sample and instrument, as well as the brightness of the X-ray source. At present, the typical resolution of these experiments is around 40 nm, but is expected to improve to 10 nm as the technique develops.

Once the diffraction pattern is phased, it can be inverted by means of a Fourier transform into a complex density function. As explained in Box 2, the amplitude and phase of the complex density can be interpreted as physical density and lattice deformation, as projected onto the **Q** vector of the Bragg peak chosen. It is clear that the method is sensitive to displacements a small fraction of a unit cell in magnitude, even though the overall resolution is relatively low. It is also obvious that a displacement of a full unit cell (or of multiple units cells) will be invisible, so a highly strained crystal will contain many $2\pi$ wraps of phase, which will have to be unwrapped if the full lattice displacement is to be resolved. The full 3D density function contains much information and is difficult to view. It is useful to examine images of isosurfaces of the density, using a single contour level, often between one-quarter and one-half of the maximum density. Such images resemble the shape of the crystal and can be compared using scanning electron microscopy (SEM), at least for isolated nanocrystals on a substrate. The shapes of individual grains of a polycrystalline material can be identified in this way, even though they are buried inside a matrix. To view the phase, it is useful to map it onto a colour scale and examine two-dimensional slices cutting through the crystal, as shown in Figs 3 and 4. To examine surface strain, it is sometimes interesting to project the colours onto the density isosurface.

The presence of strain can be discerned directly from the colour variations in these slices. An unstrained crystal will have constant phase, not necessarily zero, which is uninteresting as it arises from a trivial symmetry of the Fourier transform. A linear variation of phase is usually also disregarded because it can be attributed to false asymmetries introduced in the data by incorrect centring of the 3D data set in the computational array. Because the true centre of the Bragg peak does not usually fall exactly in the middle of one of the CCD pixels, a small centring error is inevitable and must be ignored in the images. Phase curvature is therefore the simplest form of phase structure that can be usefully interpreted as lattice deformation. Regions of positive relative phase in the crystal are due to a component of lattice displacement in the same direction as the **Q** vector, and imply a compression on the back of the crystal or a lattice expansion on the front, as viewed along **Q**.

We illustrate the imaging capabilities of the CXD method in some examples. The first, shown in Fig. 3, is the 3D imaging of Pb nanocrystals, which was the first published demonstration of the strain sensitivity[40]. The samples were grown *in situ* in APS beamline 34-ID-C by evaporation onto a $SiO_2$ substrate, melting and recrystallizing the molten droplets, then measuring 3D diffraction patterns and constructing the images shown in Fig. 3. The physical density (amplitude) of the crystal was almost constant with no defects, but there was a prominent phase feature which is attributed to an internal strain field. Figure 3 shows the strain field both as an isosurface and as a variation in colour across a cut-plane. This projection of the strain field onto the (11–1) **Q** vector could be fitted by a distribution of point 'charges' located outside the crystal. This demonstrates that the displacement field decays inside the crystal according to the Poisson equation describing continuum elasticity[35,41]. The measured strain component is apparently caused by some distribution of contact forces due to the substrate upon which the crystal is grown.

**Box 2 | Sensitivity to lattice strain.**

Illustration of how the phase in CXD images arises from the asymmetry of the diffraction pattern. For an ideal crystal, one in which the unit cells lie on a mathematically perfect 3D lattice, the intensity distribution due to the crystal shape is a periodic function of reciprocal space. The intensity distribution is identical around every Bragg peak and about the origin of reciprocal space. Overall inversion symmetry of the diffraction (Friedel's law) therefore implies that the diffraction will be locally symmetric about the exact reciprocal lattice points. This results in symmetric intensity patterns about the centre of each Bragg reflection in the CXD experiment. This is sometimes, but not always, observed in practice. When a non-symmetric pattern is seen, it can be decomposed into symmetric and antisymmetric parts. The symmetric part can be considered to come from the physical average electron density, and the antisymmetric part is associated with a real-space phase that is equal to the local displacement of the atoms from the ideal lattice, projected onto the **Q** vector of the Bragg peak concerned[62]. This displacement field is imaged as a real-space map of phase values at each position inside the sample. In general, a complex density is required to produce an asymmetric diffraction pattern. In the figure, a strained region of the crystal is illustrated as a block of material displaced from the rest by a vector $\mathbf{u}(\mathbf{r})$, which depends generally on position. The phase of the X-ray beams scattered by this block is shifted relative to that of the reference crystal by a total amount $\varphi = \mathbf{k}_f\cdot\mathbf{u} - \mathbf{k}_i\cdot\mathbf{u} = \mathbf{Q}\cdot\mathbf{u}$. Whenever Q is set to a Bragg condition, all unit-cell corners scatter in phase, so this phase shift is manifested in the final image as a region of complex density with the same magnitude as the rest of the crystal and a phase $\varphi(\mathbf{r})$.

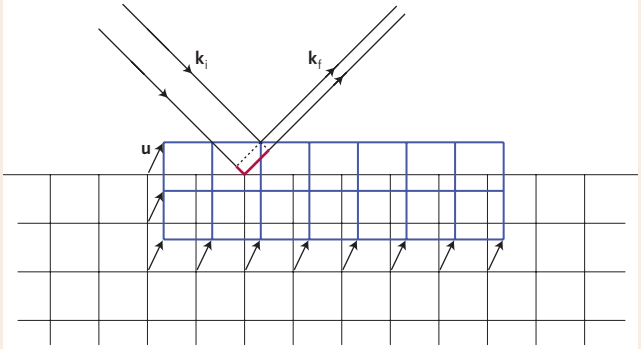


However, its propagation into the interior must, and does, obey the laws of elasticity in a defect-free isotropic medium. The maximum strain component seen is a phase shift of the complex density by +1.4 rad, corresponding to a total displacement (relative to the ideal crystal lattice) of about one-quarter of a Pb{111} spacing, or 0.08 nm (ref. 40). This is the cumulative displacement relative to the bulk at the centre of the crystal; the deviations start about 100 nm above and increase to this amount at the bottom interface with the substrate. The positive sign of the phase deviation at the back of the crystal (with respect to the direction of **Q**) indicates a compression of the lattice planes there.

A further refinement of the result came from the realization that the 700-nm size of the Pb crystal was large enough to cause a significant phase shift in the object owing to optical refraction of the X-ray beam[42]. Although much smaller in magnitude (and opposite in sign) for X-rays than for visible light, refraction corresponds to a change of phase of the wave field passing through the sample, relative to

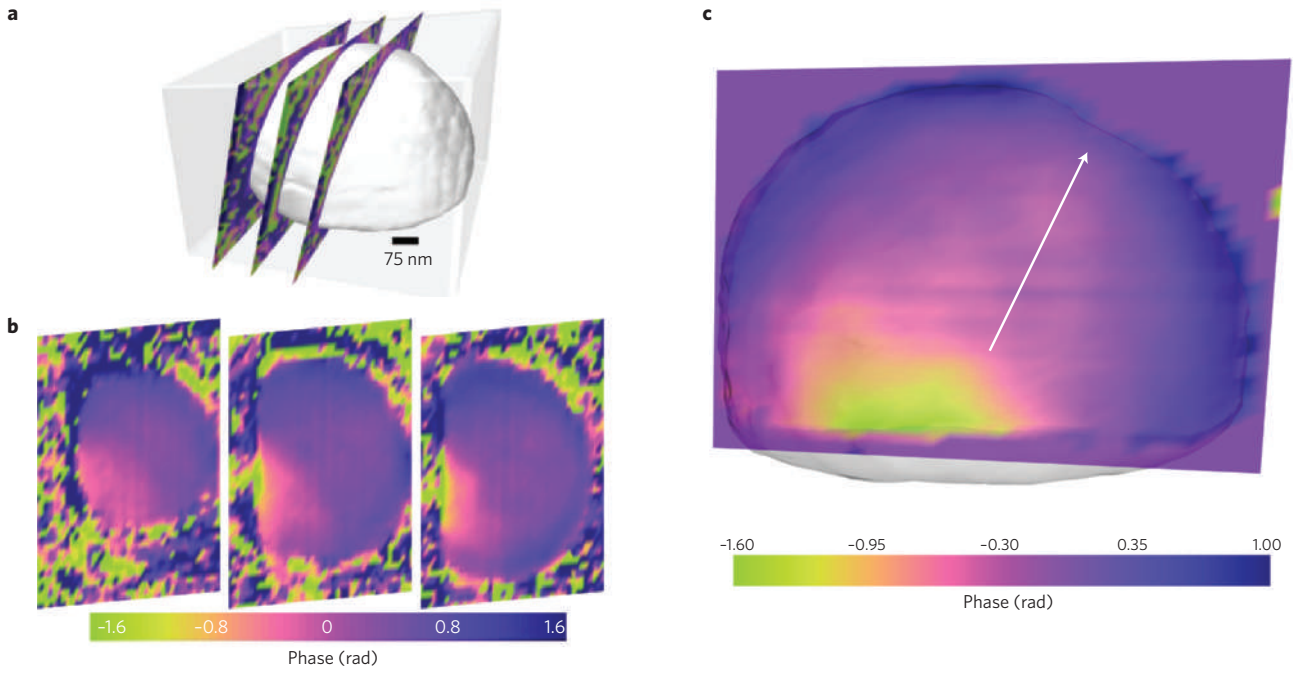


**Figure 3 | Visualization of strain inside a Pb nanocrystal. a**, Schematic showing cut-planes passing through an isosurface of the density of the Pb nanocrystal studied with CXD. **b**, The phase (in radians) is shown as colours on the extracted planes. **c**, The phase on one section of the same crystal plane after correction for refraction effects[42]. The contact strain due to the substrate is negative (green) whereas the surface strain is positive (blue). The surface strain is diminished on the (111) facet itself[42]. Parts **a** and **b** reprinted with permission from ref. 40. © 2006 NPG; part **c** reprinted with permission from ref. 42. © 2007 APS.

waves passing around it. Once corrected for this effect, which can be calculated reliably from the crystal shape and the known optical constants of Pb, the contact strain, discussed above, becomes even larger, but a new surface strain becomes visible on the facetted, spherical outer surface of the Pb nanocrystal, shown in Fig. 3c. The crystal surface is displaced in the outward direction, and therefore appears most strongly near the forward direction of **Q** (arrow in Fig. 3c). However, there is a marked reduction in magnitude on the (11−1) facet itself, seen as the flat edge lying perpendicular to **Q**. This orientation dependence is believed to be associated with the different levels of surface stress associated with the atomically flat facet and the dynamically rough curved regions of the nanocrystal[42].

The strain effects in nanocrystals and the deviations from bulk behaviour will be more pronounced for smaller crystals, where even the crystal structure itself can change[43]. It is therefore imperative to focus the coherent beam for the smallest possible size range. This is possible using Kirkpatrick–Baez mirror optics[44], Fresnel zone plates[45] or refractive lenses[46]. The lateral coherence lengths inherent to the third generation undulator sources, like ESRF or APS, are in excess of 10 μm, which is rather wasteful when studying nanometre-size objects. Focusing of a coherent beam down to 1 μm or below, which is achievable with optics that preserve the coherence in the same way as an optical lens, can improve the flux several thousand-fold. The demands on sample and beam stability are significantly increased when focusing is used.

Coherent beams have different focal properties from incoherent ones[47]. The propagation of a coherent beam is best described by its wavefronts (surfaces of constant phase) while the incoherent limit can be handled by following simple ray tracing. The full evolution of the coherent wavefront as it passes through focus needs to be described as a laterally varying phase function at each position. Near the focus, assuming ideal optics, the wave will resemble a plane wave with a Gaussian intensity profile; away from the focus it should resemble a spherical wave, converging or diverging. This plane-wave property has recently been exploited to image Au nanocrystals in the strong focus of the Fresnel zone plate at ESRF beamline ID13 (ref. 48). It has also been demonstrated that 'curved beam illumination' is advantageous for diffractive imaging[49] because the phasing (and, hence, inversion) of a diffraction pattern, using algorithms like those mentioned in Box 1, converges more rapidly. Although it appears to be true that the phase problem is easier to solve when there is no confusion with a twinned version of the object[50], the practical advantage exists only for imaging pure amplitude objects, such as shadow patterns of absorbers on a transparent substrate ('logos'). In the imaging of inherently complex objects, such as strain fields under Bragg diffraction, this advantage is lost unless some prior knowledge of the phase structure can be used to guide the phasing algorithm.

Nevertheless, there is a clear opportunity for imaging the illuminating wave field (the 'probe') using coherent diffraction. The image reconstructed from a single diffraction pattern is of the exit wave field, which is the product of the illumination wave field and the sample transmission function, both of which are generally complex. It has recently been demonstrated that if the sample can be varied systematically, as in a ptychography experiment[16], then both the probe and the sample structures can be solved simultaneously[15,51]. Figure 4a, obtained by CXD imaging of a 200-nm Au crystal using a Kirkpatrick–Baez-focused beam, shows a slight curvature of the phase within the central region of the crystal. This is unlikely to be due to strain, and could instead be an image of the curved wavefront of the focused illuminating X-ray beam, although it is not strictly possible to separate in a single measurement the phase structures of both the sample and the probe, which are superimposed.

Particularly when using a focused beam, strong radiation forces can cause the small samples to move around in the beam. To avoid sample-stability problems, nanocrystals can be grown directly on substrates or in confined geometries. Once the crystals are in intimate contact with the substrate their stability is less of an issue, and the strain, necessarily induced by the contacts, is part of the actual

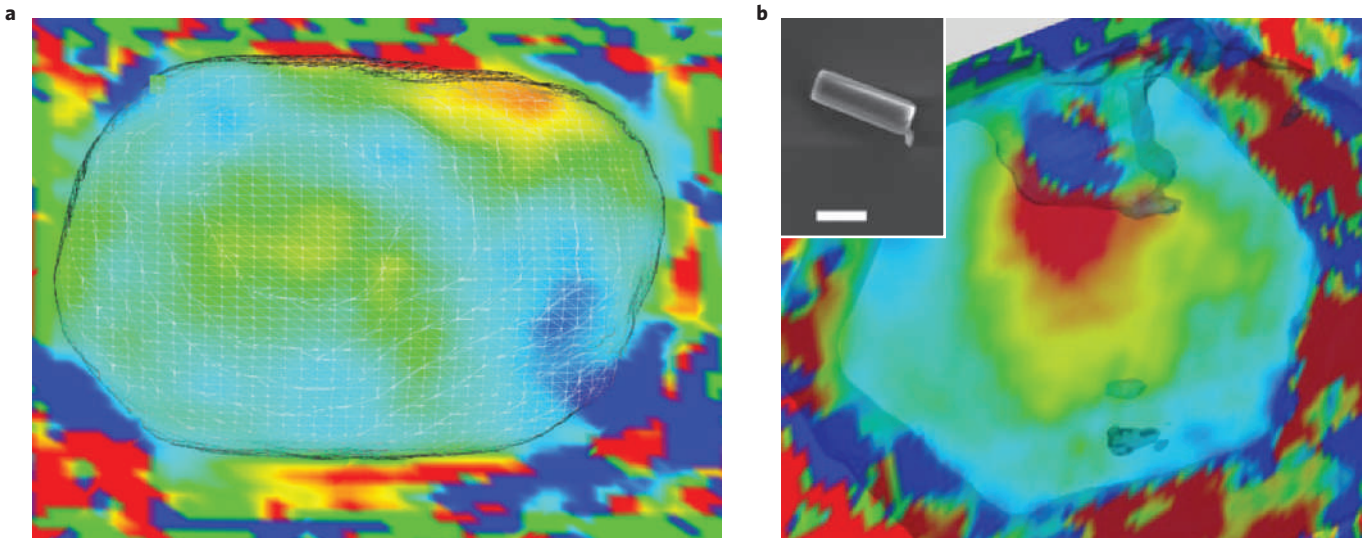


**Figure 4 | New results from CXD experiments ongoing at APS beamline 34-ID-C. a**, Phase map of a slice through a 200-nm Au nanocrystal obtained by hybrid input–output inversion of its CXD pattern measured with the {111} Bragg peak using a focused X-ray beam. **b**, Cross-section showing the phase within a hexagonal-prism ZnO crystal imaged by CXD using its 100 reflection, roughly perpendicular to one of the hexagon edges. The density isosurface, superimposed as a contour line, shows a missing region of density that may have resulted from handling with a micromanipulator. An SEM image of the crystal, 4 μm in length, is shown as an inset (scale bar is 2 μm).

subject of the investigation. The 200-nm Au nanocrystals like that shown in Fig. 4a were intimately attached to a $SiO_2$ substrate, by growing them in place, but were apparently not strained by the substrate in this case. These patterns were completely stable and found to invert reliably. A useful method of attaching crystals that are stable at high temperature to Si wafers is to overgrow a layer of amorphous $SiO_2$ by heating to 900 °C in oxygen. This method was used for the ZnO crystal shown in Fig. 4b.

As mentioned in the introduction, an important goal of the CXD method is to solve the registration problem of placing the beam on a specific crystal, instead of picking one at random. This would allow not only the parallel use of other diagnostic methods, but also measurement of multiple Bragg peaks from the same crystal; the latter would allow spatial mapping of all components of the displacement field (and, hence, strain tensor) by resolving them along different **Q** vectors. This has been attempted for the ZnO crystal whose cross-sectional phase map is shown in Fig. 4b. The crystal was dropped onto the substrate and moved with a micromanipulator to place it next to a marker cross scribed onto the substrate. In this way, a scanning electron microscope (SEM) image of the same crystal was obtained (Fig. 4b). This manipulation must have inadvertently damaged the crystal. A gash can be seen in the density contour shown and there is an associated pattern of strain localized at the tip of the damage.

## Future prospects

X-ray and electron microscopy methods complement each other in the range of sample sizes they cover best, with electrons typically giving a resolution an order of magnitude higher and a corresponding smaller field of view. The need to prepare thin samples has always been a limitation of TEM because the structures under investigation can be disturbed by the sample preparation. Traditionally, X-rays have been used only in reciprocal space, but the recent introduction of coherence-based methods at the newer synchrotron radiation sources has enabled diffraction patterns to be phased and inverted to form 'lensless' images, as we have described. Electron diffraction patterns can also be interpreted[52] or inverted[53] to obtain images of strain, again on a length scale smaller than the corresponding X-ray work.

X-ray methods are especially well suited to *in situ* measurement of materials within a working environment. Because the interesting mechanical properties of nanoscale materials are more associated with their unusual strength[5], it is important to examine them under working conditions, especially those that lead to their breakdown. It is therefore expected that these X-ray strain imaging methods will find widespread application to nanomaterials under extreme temperatures and pressure, as components of electronic or micromechanical devices, under deformation, and in extreme chemical environments. The methods will be used to great effect to study the pattern formation that is associated with materials synthesis on the nanometre scale. The self-limiting growth associated with self-assembly in the presence of surfactants is an obvious example[54]. The most exciting direction will probably be ultrafast imaging of shock waves in nanocrystals when the new X-ray free-electron lasers become operational.

## References

1. Pauling, L. *The Nature of the Chemical Bond, and the Structure of Molecules and Crystals* (Cornell Univ. Press, 1960).
2. Buffat, P. & Borel, J.-P. Size effect on the melting temperature of gold particles. *Phys. Rev. A* **13,** 2287–2297 (1975).
3. Madey, T. E., Chen, W., Wang, H., Kaghazchi, P. & Jacob, T. Nanoscale surface chemistry over faceted substrates: structure, reactivity and nanotemplates. *Chem. Soc. Rev.* **37,** 2310–2327 (2008).
4. Yu, H., Li, J. B., Loomis, R. A., Wang, L. W. & Buhro, W. E. Two- versus three-dimensional quantum confinement in indium phosphide wires and dots. *Nature Mater.* **2,** 517–520 (2003).
5. Hodge, A. M. *et al.* Scaling equation for yield strength of nanoporous open-cell foams. *Acta Math.* **55,** 1343–1349 (2007).
6. Fritz, D. M. *et al.* Ultrafast bond softening in bismuth: Mapping a solid's interatomic potential with X-rays. *Science* **315,** 633–636 (2007).
7. Vartanyants, I. A. *et al.* Coherent X-ray scattering and lensless imaging at the European XFEL facility. *J. Synchrotron Radiat.* **14,** 453–470 (2007).
8. McCartney, M. R. & Smith, D. J. Electron holography: Phase imaging with nanometer resolution. *Annu. Rev. Mater. Res.* **37,** 729–767 (2007).
9. Midgley, P. A. & Dunin-Borkowski, R. E. Electron tomography and holography in materials science. *Nature Mater.* **8,** 271–280 (2009).
10. Kim, M., Zuo, J. M. & Park, G. S. High-resolution strain measurement in shallow trench isolation structures using dynamic electron diffraction. *Appl. Phys. Lett.* **84,** 2181–2183 (2004).
11. Urban, K. W. Studying atomic structures by aberration-corrected transmission electron microscopy. *Science* **321,** 506–511 (2008).

12. Varela, M. *et al.* Materials characterization in the aberration corrected scanning transmission electron microscope. *Annu. Rev. Mater. Res.* **35,** 539–569 (2005).
13. Hytch, M., Houdellier, F., Hue, F. & Snoeck, E. Nanoscale holographic interferometry for strain measurements in electronic devices. *Nature* **453,** 1086–1089 (2008).
14. Ade, H. & Stoll, H. Near-edge X-ray absorption fine-structure microscopy of organic and magnetic materials. *Nature Mater.* **8,** 281–290 (2009).
15. Thibault, P. *et al.* High-resolution scanning X-ray diffraction microscopy. *Science* **321,** 379–382 (2008).
16. Rodenburg, J. M. *et al.* Hard-X-ray lensless imaging of extended objects. *Phys. Rev. Lett.* **98,** 034801 (2007).
17. Larson, B. C., Yang, W., Ice, G. E., Budai, J. D. & Tischler, J. Z. Three-dimensional X-ray structural microscopy with submicrometre resolution. *Nature* **415,** 887–890 (2002).
18. Schmidt, S. *et al.* Watching the growth of bulk grains during recrystallization of deformed metals. *Science* **305,** 229–232 (2004).
19. Ice, G. E. & Larson, B. C. Three-dimensional X-ray structural microscopy using polychromatic microbeams. *Mater. Res. Soc. Bull.* **29,** 170–176 (2004).
20. Miao, J. W., Charalambous, P., Kirz, J. & Sayre, D. Extending the methodology of X-ray crystallography to allow imaging of micrometre-sized non-crystalline specimens. *Nature* **400,** 342–344 (1999).
21. Metzger, T. H., Schulli, T. U. & Schmidbauer, M. X-ray methods for strain and composition analysis in self-organized semiconductor nanostructures. *C. R. Phys.* **6,** 47–59 (2005).
22. Krause, B. *et al.* Shape, strain, and ordering of lateral InAs quantum dot molecules. *Phys. Rev. B* **72,** 085339 (2005).
23. Plantevin, O., Gago, R., Vazquez, L., Biermanns, A. & Metzger, T. H. In situ X-ray scattering study of self-organized nanodot pattern formation on GaSb(001) by ion beam sputtering. *Appl. Phys. Lett.* **91,** 113105 (2007).
24. Malachias, A. *et al.* X-ray study of atomic ordering in self-assembled Ge islands grown on Si(001). *Phys. Rev. B* **72,** 165315 (2005).
25. Richard, M. I. & Metzger, T. H. Defect cores investigated by X-ray scattering close to forbidden reflections in silicon. *Phys. Rev. Lett.* **99,** 225504 (2007).
26. Malachias, A., Metzger, T. H., Stoffel, M., Schmidt, O. G. & Holy, V. Composition and atomic ordering of Ge/Si(001) wetting layers. *Thin Solid Films* **515,** 5587–5592 (2007).
27. Brehm, M. *et al.* Quantitative determination of Ge profiles across SiGe wetting layers on Si (001). *Appl. Phys. Lett.* **93,** 121901 (2008).
28. Matthews, J. W. & Blakeslee, A. E. *J. Cryst. Growth* **32,** 265–273 (1976).
29. Fiory, A. T., Bean, J. C., Feldman, L. C. & Robinson, I. K. Commensurate and incommensurate structures in molecular beam epitaxially grown $Ge_xSi_{1-x}$ films on Si(100). *J. Appl. Phys.* **56,** 1227–1229 (1984).
30. Kegel, I. *et al.* Determination of strain fields and composition of self-organized quantum dots using X-ray diffraction. *Phys. Rev. B* **63,** 035318 (2001).
31. Malachias, A. *et al.* 3D composition of epitaxial nanocrystals by anomalous x-ray diffraction: Observation of a Si-rich core in Ge domes on Si(100). *Phys. Rev. Lett.* **91,** 176101 (2003).
32. Zhong, Z., Chen, P., Jiang, Z. & Bauer, G. Temperature dependence of ordered GeSi island growth on patterned Si(001) substrates. *Appl. Phys. Lett.* **93,** 043106 (2008).
33. Gailhanou, M. *et al.* Strain field in silicon on insulator lines using high resolution X-ray diffraction. *Appl. Phys. Lett.* **90,** 111914 (2007).
34. Lagally, M. G. & Rugheimer, P. P. Strain engineering in germanium quantum dot growth on silicon and silicon-on-insulator. *Jpn. J. Appl. Phys.* **41,** 4863–4866 (2002).
35. Prevot, G. & Croset, B. Elastic relaxations and interactions on metallic vicinal surfaces: Testing the dipole model. *Phys. Rev. B* **74,** 235410 (2006).
36. Eberlein, M. *et al.* Investigation by high resolution X-ray diffraction of the local strains induced in Si by periodic arrays of oxide filled trenches. *Phys. Status Solidi A* **204,** 2542–2547 (2007).
37. Minkevich, A. A. *et al.* Inversion of the diffraction pattern from an inhomogeneously strained crystal using an iterative algorithm. *Phys. Rev. B* **76,** 104106 (2007).
38. Sutton, M. *et al.* Observation of speckle by diffraction with coherent X-rays. *Nature* **352,** 608–610 (1991).
39. Miao, J. & Sayre, D. On possible extensions of X-ray crystallography through diffraction-pattern oversampling. *Acta Crystallogr. A* **56,** 596–605 (2000).
40. Pfeifer, M. A., Williams, G. J., Vartanyants, I. A., Harder, R. & Robinson, I. K. Three-dimensional mapping of a deformation field inside a nanocrystal. *Nature* **442,** 63–66 (2006).
41. Landau, L. & Lifshitz, E. *Theory of Elasticity* (Pergamon, 1986).
42. Harder, R., Pfeifer, M. A., Williams, G. J., Vartaniants, I. A. & Robinson, I. K. Orientation variation of surface strain. *Phys. Rev. B* **76,** 115425 (2007).
43. Marks, L. D. Experimental studies of small particle structures. *Rep. Prog. Phys.* **57,** 603–649 (1994).
44. Kirkpatrick, P. & Baez, A. V. Formation of optical images by X-rays. *J. Opt. Soc. Am.* **38,** 766–774 (1948).
45. Jefimovs, K. *et al.* Fabrication of Fresnel zone plates for hard X-rays. *Microelectr. Engineer.* **84,** 1467–1470 (2007).
46. Snigirev, A., Kohn, V., Snigireva, I. & Lengeler, B. A compound refractive lens for focusing high-energy X-rays. *Nature* **384,** 49–51 (1996).
47. Born, M. & Wolf, E. *Principles of Optics* 7th edn (Cambridge Univ. Press, 1999).
48. Schroer, C. G. *et al.* Coherent X-ray diffraction imaging with nanofocused illumination. *Phys. Rev. Lett.* **101,** 090801 (2008).
49. Abbey, B. *et al.* Keyhole coherent diffractive imaging. *Nature Phys.* **4,** 394–398 (2008).
50. Williams, G. J. *et al.* Fresnel coherent diffractive imaging. *Phys. Rev. Lett.* **97,** 025506 (2006).
51. Quiney, H. M., Peele, A. G., Cai, Z., Paterson, D. & Nugent, K. A. Diffractive imaging of highly focused X-ray fields. *Nature Phys.* **2,** 101–104 (2006).
52. Huang, W. J. *et al.* Coordination-dependent surface atomic contraction in nanocrystals revealed by coherent diffraction. *Nature Mater.* **7,** 308–313 (2008).
53. Zuo, J. M., Vartanyants, I., Gao, M., Zhang, R. & Nagahara, L. A. Atomic resolution imaging of a single double-wall carbon nanotube from diffraction intensities. *Science* **300,** 1419–1421 (2003).
54. Murray, C. B. Colloidal synthesis of nanocrystals and nanocrystal superlattices. *IBM J. Res. Dev.* **45,** 47–56 (2001).
55. Marchesini, S. *et al.* X-ray image reconstruction from a diffraction pattern alone. *Phys. Rev. B* **68,** 140101 (2003).
56. Sayre, D. Some implications of a theorem due to Shannon. *Acta Crystallogr.* **5,** 843–843 (1952).
57. Shannon, C. Communication in the presence of noise. *Proc. Inst. Radio Engineers* **37,** 10–21 (1949).
58. Bates, R. H. T. Fourier phase problems are uniquely solvable in more than one dimension. 1. Underlying theory. *Optik* **61,** 247–262 (1982).
59. Fienup, J. R. Phase retrieval algorithms: a comparison. *Appl. Opt.* **21,** 2758–2769 (1982).
60. Williams, G. J., Pfeifer, M. A., Vartanyants, I. A. & Robinson, I. K. Effectiveness of iterative algorithms in recovering phase in the presence of noise. *Acta Crystallogr. A* **63,** 36–42 (2007).
61. Vartanyants, I. A., Pitney, J. A., Libbert, J. L. & Robinson, I. K. Reconstruction of surface morphology from coherent X-ray reflectivity. *Phys. Rev. B* **55,** 13193–13202 (1997).
62. Vartanyants, I. A. & Robinson, I. K. Partial coherence effects on the imaging of small crystals using coherent X-ray diffraction. *J. Phys. Condens. Matter* **13,** 10593–10611 (2001).


## Acknowledgements

We acknowledge the collaboration of M. Watari, M. Newton, S. J. Leake, R. A. McKendry and G. Aeppli in the experimental work presented in Fig. 4. That previously unpublished research was supported by a Royal Society Wolfson Award, a European Seventh Framework Programme Advanced Grant and the Engineering and Physical Sciences Research Council grant EP/D052939/1. The CXD instrumentation, based at APS beamline 34-ID-C, was built with US National Science Foundation grant DMR-9724294 and supported by the Materials Research Laboratory of the University of Illinois under US Department of Energy (DOE) contract DEFG02-91ER45439. The APS is operated by the US DOE contract number W 31 109 ENG 38.